ACS APPLIED MATERIALS & INTERFACES

Research Article

www.acsami.org

Novel Method for Controllable Fabrication of a Superhydrophobic CuO Surface on AZ91D Magnesium Alloy

Zuxin She, Qing Li,* Zhongwei Wang, Longqin Li, Funan Chen, and Juncen Zhou

School of Chemistry and Chemical Engineering, Southwest University, Chongqing 400715, P.R. China

ABSTRACT: A novel method for controllable fabrication of a superhydrophobic CuO surface on AZ91D magnesium alloy is reported in this paper. Hierarchical structure composed of micro/nano-featherlike CuO was obtained by electrodeposition of Cu−Zn alloy coating and subsequently an electrochemical anodic treatment in alkaline solution. After modification with lauric acid, the surface became hydrophobicity/superhydrophobicity. The formation of featherlike CuO structures was controllable by varying the coating composition. By applying SEM, ICP-AES, and water contact angle analysis, the effects of coating composition on the surface morphology and hydrophobicity of the as-prepared surfaces were detailedly studied. The results indicated that at the optimal condition, the surface showed a good superhydrophobicity with a water contact angle as high as 155.5 ± 1.3° and a sliding angle as low as about 3°. Possible growth mechanism of featherlike CuO hierarchical structure was discussed. Additionally, the anticorrosion effect of the superhydrophobic surface was studied by potentiodynamic polarization and electrochemical impedance spectroscopy (EIS) measurements. The interface model for anticorrosion mechanism of superhydrophobic surface in corrosive medium was proposed. Besides, the mechanical stability test indicated that the resulting superhydrophobic surfaces have good mechanical stability.

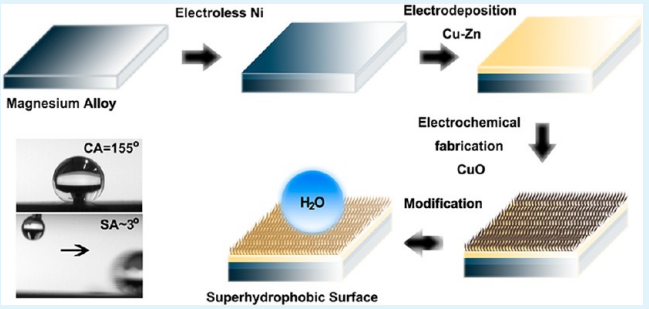

KEYWORDS: *superhydrophobic surface, controllable, featherlike structures, CuO, anticorrosion, interface model*

1. INTRODUCTION

Ever since the famous lotus effect was reported, superhydrophobic surfaces with a water contact angle (CA) greater than 150° and a sliding angle (SA) less than 10° have attracted tremendous interest from researchers because of their various special applications in self-cleaning,[1−3] anti-contamination,[4] anti-icing,[5,6] and anticorrosion.[7,8] Up to now, numerous methods are developed for fabricating superhydrophobic surfaces, such as electrochemical deposition,[9,10] sol−gel method,[11,12] solution-immersion process,[13−15] chemical etching,[16,17] self-assembly technique,[18,19] spraying method,[20] and so on.

Many studies have been focused on the preparation of superhydrophobic CuO surfaces by means of various methods owing to its interesting structures such as candock-like, chrysanthemum-like, and dandelion-like structures etc..[21] For instance, Pei' group fabricated a superhydrophobic CuO film with dandelionlike structure on copper plate via a low-pressure-oxidation method.[22] Liu et al.[23] and Zhang et al.[24] reported a superhydrophobic CuO surface with microcabbage and flower-like structures on Cu foils through solution-immersion method, respectively. Wang' group prepared a superhydrophobic surface with hierarchical nanowire CuO structure on Cu plate via oxygen adsorption.[25] However, all these rough structures were formed on copper substrate and the preparation processes were time-consuming, requiring expensive reagents or special equipment to carry out. Therefore, it could be desirable to design a novel method for fabricating superhydrophobic CuO surface.

Magnesium alloys as important engineering materials have been received much attention in the automobile, aircraft and aerospace industries due to their low density, high specific strength and stiffness and excellent castability, machinability.[26−29] However, the large-scale application is limited due to their poor corrosion resistance. Then it is significant to prepare a self-cleaning and anticorrosion superhydrophobic surface for wide application of magnesium alloy. Moreover, to the best of our knowledge, there was no report on the preparation of superhydrophobic CuO surface based on magnesium alloy.

In this paper, we design a method for fabricating superhydrophobic CuO surface on magnesium alloy. The schematic illustration is exhibited in Scheme 1. The fabrication process of superhydrophobic surface mainly contains four steps: electroless Ni, electrodeposition of Cu−Zn, electrochemical fabrication of CuO and modification. The whole process was facile to carry out and did not require expensive reagents and complex equipment, which made this method widely applicable and easy for large-area production.

Received: June 3, 2012
Accepted: July 30, 2012
Published: July 30, 2012

 © 2012 American Chemical Society

Scheme 1. Schematic Illustration of Fabricating a Superhydrophobic Surface and CA, SA Images of As-Prepared Superhydrophobic CuO Surface

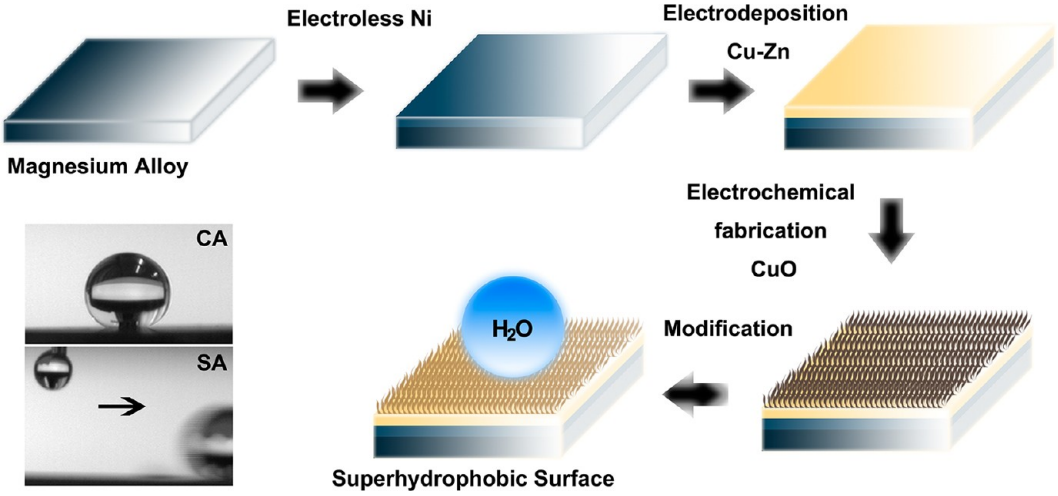

2. MATERIALS AND METHODS

2.1. Materials. All the reagents were analytical grade and Milli-Q water was used throughout the experiments. AZ91D magnesium alloy with a chemical composition (wt %) of Mg-8.77Al-0.74Zn was used in this study. The dimensions of all samples were 45 mm ×18 mm ×4 mm. A copper bar (purity >99.8%) or a brass bar (Cu 70 wt %, Zn 30 wt %) was set as the counter electrode in electrodeposition process, and a graphite electrode was set as the cathode in electrochemical preparation of CuO and modification, respectively.

2.2. Pretreatment of Magnesium Alloy. The AZ91D substrate was polished with SiC paper of successively finer grit down to 1500 grit, rinsed with deionized water, ultrasonically degreased in acetone and dried in air, degreased in an alkaline solution containing 0.25 g L^{-1} NaOH, 20 g L^{-1} Na_2CO_3, and 0.5 g L^{-1} $C1_2H_{25}NaSO_4$ at 70 °C for 5 min, and then rinsed with deionized water. To remove the oxide film from the magnesium alloy surface, the pretreated magnesium alloy was immersed in an acid solution containing 5 mL L^{-1} HNO_3 (65.0 wt %), 15 mL L^{-1} H_3PO_4 (85.0 wt %), 50 mL L^{-1} CH_3CH_2OH, and 0.5 g L^{-1} $Mn(H_2PO_4)_2$, for 2 min at room temperature.

2.3. Electroless Nickel Plating. Because of the high activity, the magnesium alloy must be pre-treated before electrodeposition of Cu or Cu−Zn. In this paper, Ni electroless plating was used as pretreatment technology. The optimized bath contained 10 g L^{-1} $Ni_2(OH)_2CO_3$, 5 g L^{-1} $C_6H_8O_7{\cdot}H_2O$, 0.001 g L^{-1} CH_4N_2S, 20 g L^{-1} $NaH_2PO_2{\cdot}H_2O$, and 30 mL L^{-1} $NH_3{\cdot}H_2O$, and the pH value of the bath was 6.2-6.4. The plating time was 60 min at 75 °C.

2.4. Electrodeposition of Cu and Cu−Zn Coatings. The Cu and Cu−Zn coatings were electrodeposited using electrochemical workstation (CorrTest CS350) under direct current conditions after electroless Ni plating. The bath mainly contained $CuSO_4{\cdot}5H_2O$, $ZnSO_4{\cdot}7H_2O$ and $NaKC_4O_6H_4$. In order to control the coating composition, the total concentration of Zn^{2+} and Cu^{2+} in bath remained unchanged at 0.169 mol L^{-1}, although the molar ratio of Zn^{2+} to Cu^{2+} was changed from 0:1 to 5:1. The specific bath compositions and detailed parameters are given in Table 1. And the copper bar was used as anode in Bath 1; brass bar was used as anode in Bath 2 to 5.

2.5. Electrochemical Anodic Preparation of CuO Film. The magnesium alloy with pure Cu or Cu−Zn coating (as anode) was immersed in 4.0 M NaOH with current density about 600 mA dm^{-2} supplied by direct current supply (Ruidian RZ-530) at 60 °C for 10 min.

2.6. Modification. By using electrostatic absorption to enhance the efficiency of modification, the sample with CuO film (as anode) was immersed into an ethanolic lauric acid solution (0.01 M) under a DC voltage of 15 V supplied by direct current supply at room temperature for 10 min.

Table 1. Bath Compositions and Operating Conditions for Electrodeposition of Cu and Cu−Zn Coating[a]

bath no.	Zn^{2+}/Cu^{2+} ratio	C_{CuSO_4} (g L^{-1})	C_{ZnSO_4} (g L^{-1})	others (g L^{-1})
1	0:1	42	0	
2	0.4:1	30	14	$NaKC_4O_6H_4$: 100
3	1:1	20	24	$Na_3C_6H_5O_7{\cdot}2H_2O$: 20
4	2.5:1	12	34	Na_2SO_4: 20
5	5:1	7	40	

[a]Conditions: current density, 600 mA dm^{-2}; pH 13.0−13.5; temperature, 35 °C; time, 60 min.

2.7. Characterization and Tests. The water contact angle and sliding angle were measured with a water drop volume of 10 μL using an optical contact angle meter (POWEREACH JC2000C1) at ambient temperature. The advancing angle (θ_A) and receding angle (θ_R) were measured according to the previous report.[30,31] The values reported are averages of five measurements made on different positions of the sample surface. SEM images were obtained on a scanning electron microscope (SEM; HITACHI S-4800). The coatings were also analyzed by X-ray diffractometer (XRD; Purkinje General Instrument XD-3) using Cu KR radiation (λ = 0.15406 nm), inductively coupled plasma atomic emission spectrometry (ICP-AES; Purkinje General Instrument TPS-7000) and X-ray photoelectron spectroscopy (XPS; Thermo ESCALAB 250). The mechanical stability of resulting sample was measured by a digital microhardness tester (MHV 2000).

The anticorrosion effect was evaluated by means of potentiodynamic polarization and electrochemical impedance spectroscopy (EIS) tests using a classical three electrodes cell with platinum as counter electrode, saturated calomel electrode (SCE, +0.242 V *vs.* SHE) as reference electrode, and the samples with an exposed area of 1 cm^2 as working electrode in neutral 3.5 wt % NaCl solution. The potentiodynamic polarization curves were performed by electrochemical workstation (CorrTest CS350) with a constant voltage scan rate of 1 mV s^{-1}. The electrochemical impedance spectroscopy (EIS) was performed with CS350 Electrochemical Workstation. The employed amplitude of sinusoidal signal was 10 mV, and the frequency range studied was from 1×10^5 to 1×10^{-2} Hz. The test temperature was room temperature. All the electrochemical corrosion tests were normally repeated at least three times under the same conditions, checking that they presented reasonable reproducibility.

dx.doi.org/10.1021/am3009949 | ACS Appl. Mater. Interfaces 2012, 4, 4348−4356

3. RESULTS AND DISCUSSION

3.1. Fabrication of Superhydrophobic Surface. Figure 1 shows the XRD patterns of the corresponding samples before

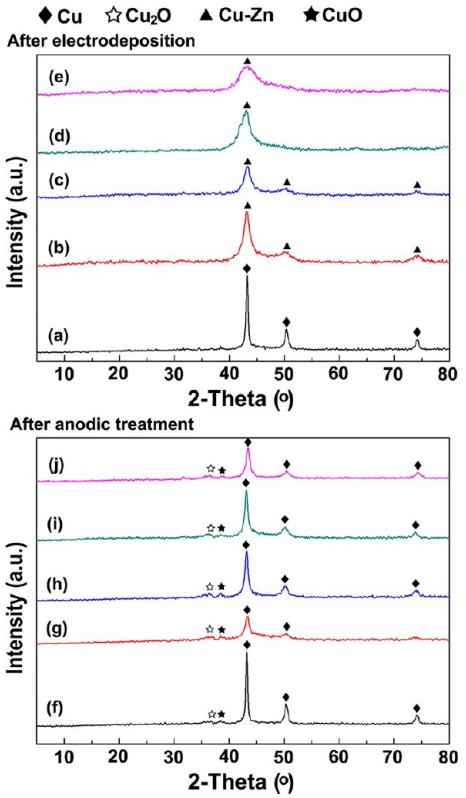

Figure 1. XRD patterns of the samples after electrodeposition, after anodic treatment at different molar ratios of Zn^{2+} to Cu^{2+}: (a, f) 0:1, (b, g) 0.4:1, (c, h) 1:1, (d, i) 2.5:1, (e, j) 5:1.

and after electrodeposition at different molar ratios of Zn^{2+} to Cu^{2+}. It can be easily seen that there are characteristic peaks for pure Cu in Figure 1a and the three diffraction peaks can be indexed to the face-center cubic Cu in JCPDS Card No.04-0836. When the molar ratio of Zn^{2+} to Cu^{2+} was increased, the diffraction peaks for Cu became weaker and the diffraction peaks were gradually transformed from characteristic peaks for pure Cu to Cu−Zn alloy. The peak positions for Cu−Zn alloy as shown in Figure 1b and c were consistent with the pure Cu, which could be ascribed to the fact that the deposition of Cu and Zn occurred simultaneously in codeposition, leading to that crystal lattice in Cu matrix was replaced by Zn partly and formed substitutional solid solution. For Figure 1d and e, when crystal lattice in Cu matrix was replaced by many Zn, the XRD patterns showed the diffraction peaks of Cu−Zn alloy. The peak positions for Cu−Zn alloy were consistent with the previous literatures.[32,33] ICP-AES was applied to confirm the exactitude composition of coatings. Figure 2 shows the relationship between Zn content in coating and the molar ratio of Zn^{2+} to Cu^{2+} in bath. It could be seen that the Zn content in coating increased with the increase of Zn^{2+} in the bath. This result is in conformity with the XRD result.

Additionally, after electrochemical anodic treatment, it is obviously shown that each curve of Figure 1f−j contains diffraction peaks for CuO, Cu_2O, and Cu, and all diffraction peak positions for CuO and Cu_2O are consistent with the previous reports.[34−36] After anodic treatment the peaks became

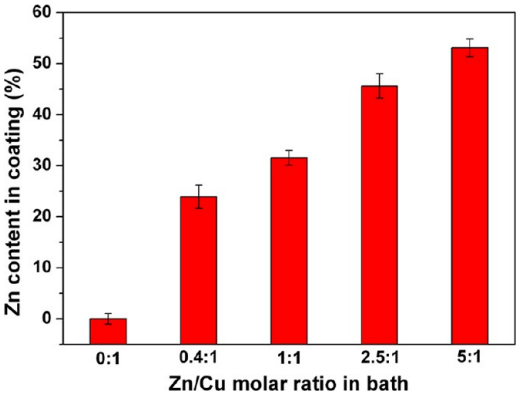

Figure 2. Relationship between the Zn content in coating and the molar ratio of Zn^{2+} to Cu^{2+} in bath.

sharper compared with that before anodic treatment and the peak intensities of Cu increased obviously, which could be ascribed that Zn in Cu−Zn alloy coating was dissolved under a high anodic potential and strong base in anodic treatment process. These weak diffraction peaks for CuO indicated that only a small number of CuO particles were formed on the surface of the sample in electrochemical anodic treatment.

Besides, CuO and Cu_2O were further confirmed by XPS analysis. Figure 3 shows the XPS spectra of the sample after

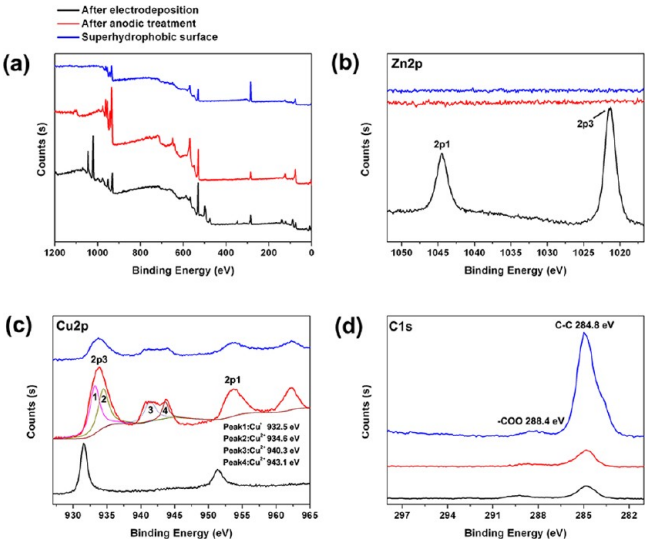

Figure 3. XPS spectra of the sample after electrodeposition, after anodic treatment and after modification (the superhydrophobic surface). The sample was prepared under optimal conditions.

electrodeposition (the molar ratio of Zn^{2+} to Cu^{2+} was 2.5:1 in bath), after anodic treatment and after modification. From Figure 3a−c, it can be observed that the sample surface after electrodeposition exhibited the Zn peaks (1021.8 eV, 1044.8 eV) and the Cu peaks (932.6 eV, 952.2 eV), indicating that Cu−Zn alloy coating deposited on the substrate. Evidently, the Zn peaks disappeared after anodic treatment, which was consistent with the XRD analysis result shown in Figure 1g−j. From panels a and c in Figure 3, the relative amounts of CuO and Cu_2O formed in anodic treatment allowed the previous XRD analysis, according to the previous reports,[37−40] In the XPS spectra of the superhydrophobic surface (Figure 3a and d), a strong C1s can be easily observed, which means that the lauric

dx.doi.org/10.1021/am3009949 | ACS Appl. Mater. Interfaces 2012, 4, 4348−4356

acid was deposited on the surface. At the same time, the peak signal at 288.4 eV was the indication of the presence of −COO.[41]

The surface compositions and morphologies with different anodizing times under the optimal condition were investigated by XRD and SEM. Before anodizing treatment, the diffraction peak of Cu−Zn alloy is observed (Figure 4e) and the surface is

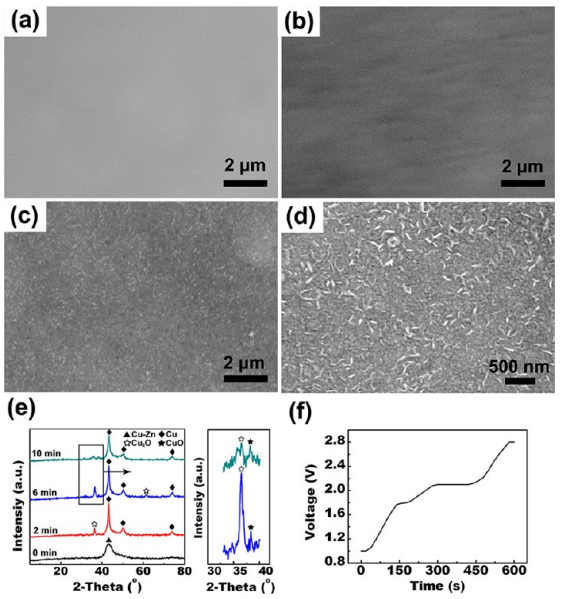

Figure 4. SEM images of Cu−Zn coating with different anodizing times: (a) 0, (b) 2, and (c) 6 min, and (d) 6 min at high magnification; (e) XRD patterns of surfaces with different anodizing times; (f) The voltage−time curve. The coatings were prepared from the 2.5:1 Zn^{2+}:Cu^{2+} molar ratio in bath).

smooth (Figure 4a). It is noteworthy that after 2 min, the surface morphology has some changes (Figure 4b) and the XRD pattern indicates that Cu and Cu_2O appeared on the surface. When the anodic time was 6 min, the surface is uniformly and completely covered by countless particles (Figure 4c). It is obvious from the higher magnification SEM image (Figure 4d), that the surface morphology consists of countless small CuO featherlike structures, which is similar to that shown in Figure 6g, h (the anodic time is 10 min). These SEM images indicate that the featherlike CuO structures were formed gradually as the anodic treatment time prolonging.

In addition, the voltage−time curve of the formation process of CuO film is exhibited in Figure 4f. The potential gradually increased because poorly conductive oxidation products formed on the surface as time prolonging.

3.2. Wetting Behaviors. The wetting behaviors of the resulting surfaces prepared at different molar ratios of Zn^{2+} to Cu^{2+} were analyzed by water contact angle and contact angle hysteresis.[42] Static contact angle and contact angle hysteresis at different molar ratios of Zn^{2+} to Cu^{2+} are shown in Figure 5a, b. It is obvious that the resulting surfaces showed different hydrophobicities from panels a and b in Figure 5. The contact angles of the resulting surfaces firstly increased from 137.1 ± 2.4° to 148.3 ± 2.1° with the increase of molar ratio of Zn^{2+} to Cu^{2+}, and reached the maximum value of 155.5 ± 1.3° at the molar ratio of 2.5:1, finally it decreased to 140.4 ± 3.3°. Meanwhile, we can find that the contact angle hysteresis showed the opposite change to that of the contact angle

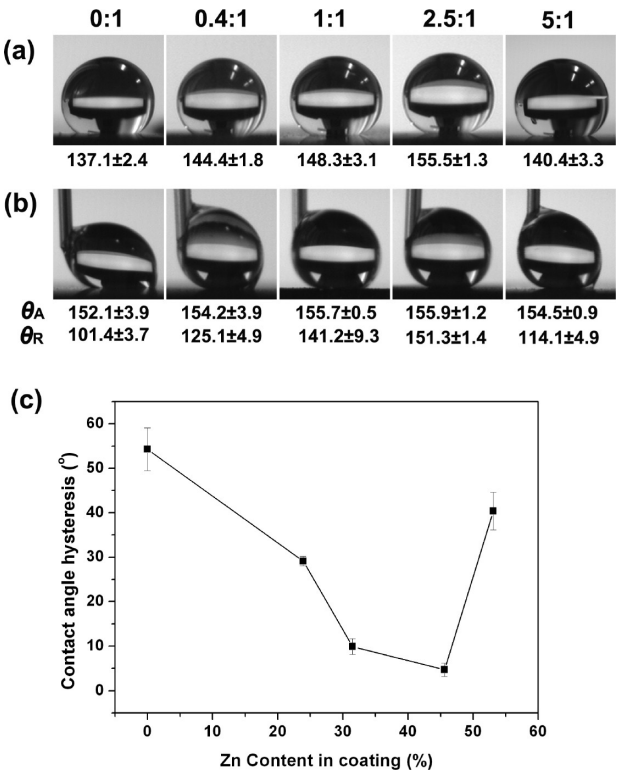

Figure 5. (a) Static contact angle and (b) advancing/receding contact angle at different molar ratios of Zn^{2+} to Cu^{2+}; (c) relationship between contact angle hysteresis and the Zn content in coating.

(Figure 5b). The analysis showed that the contact angle hysteresis decreased when the contact angle increased. When the surface became superhydrophobicity, the contact angle hysteresis would decrease to a minimum value. This result also can be seen in Figure 5c. The resulting superhydrophobic surface possessed the lowest contact angle hysteresis of 4.7 ± 0.3° at the Zn content of 45.6 ± 2.4%. It therefore revealed that the surface with a contact angle of 155.5 ± 1.3° and a contact angle hysteresis of 4.7 ± 0.3° showed a good superhydrophobicity at the Zn content of 45.6 ± 2.3% and corresponded to the molar ratio of Zn^{2+} to Cu^{2+} of 2.5:1. Moreover, sliding angle of the as-prepared superhydrophobic surface was tested and the value was about 3°. The SA images of as-prepared superhydrophobic surface are exhibited in Scheme 1.

To obtain a better understanding of the change of CA, weused SEM. Figure 6 shows the surface morphologies of CuO films prepared at different molar ratios of Zn^{2+} to Cu^{2+} with different magnifications. As shown in Figure 6, it can be easily found that all the surfaces were composed of featherlike CuO microstructures and the size of CuO gradually decreased with the increase of molar ratio of Zn^{2+} to Cu^{2+}, leading to the decrease of surface roughness. The size of featherlike microstructures (Figure 6a and i) was the largest and the smallest, exhibiting the largest and the smallest surface roughness, respectively. Both the oversized roughness and undersized roughness would lead to a smaller contact angle. For Figure 6c, the surface was covered by the unevenly distributed CuO so led to a relatively large contact angle. Images e and g in Figure 6 show that the surfaces have a relatively appropriate roughness, but in Figure 6e, some CuO of large size were unevenly distributed on the surface. Amazingly, the surface

dx.doi.org/10.1021/am3009949 | ACS Appl. Mater. Interfaces 2012, 4, 4348−4356

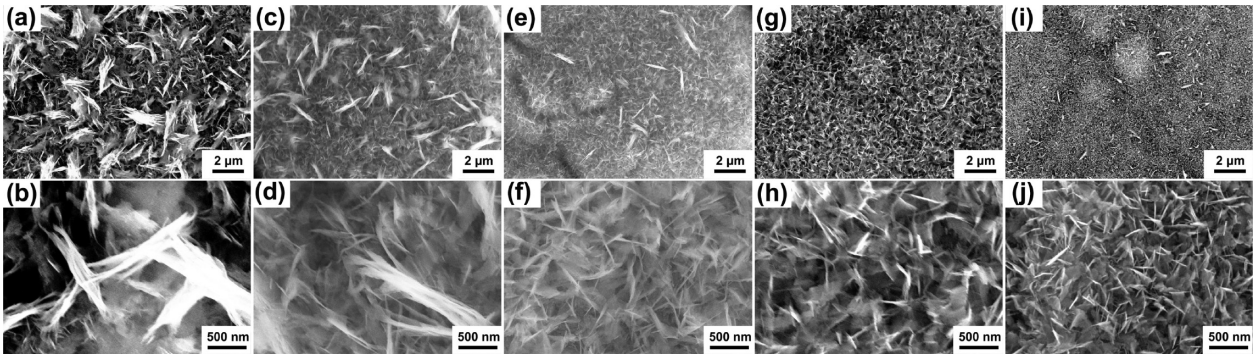

Figure 6. Surface morphologies of CuO films at different molar ratios of Zn^{2+} to Cu^{2+}: (a, b) 0:1, (c, d) 0.4:1, (e, f) 1:1, (g, h) 2.5:1, and (i, j) 5:1.

Scheme 2. Illustration of Possible Growth Mechanism for Controllable Featherlike CuO Architectures

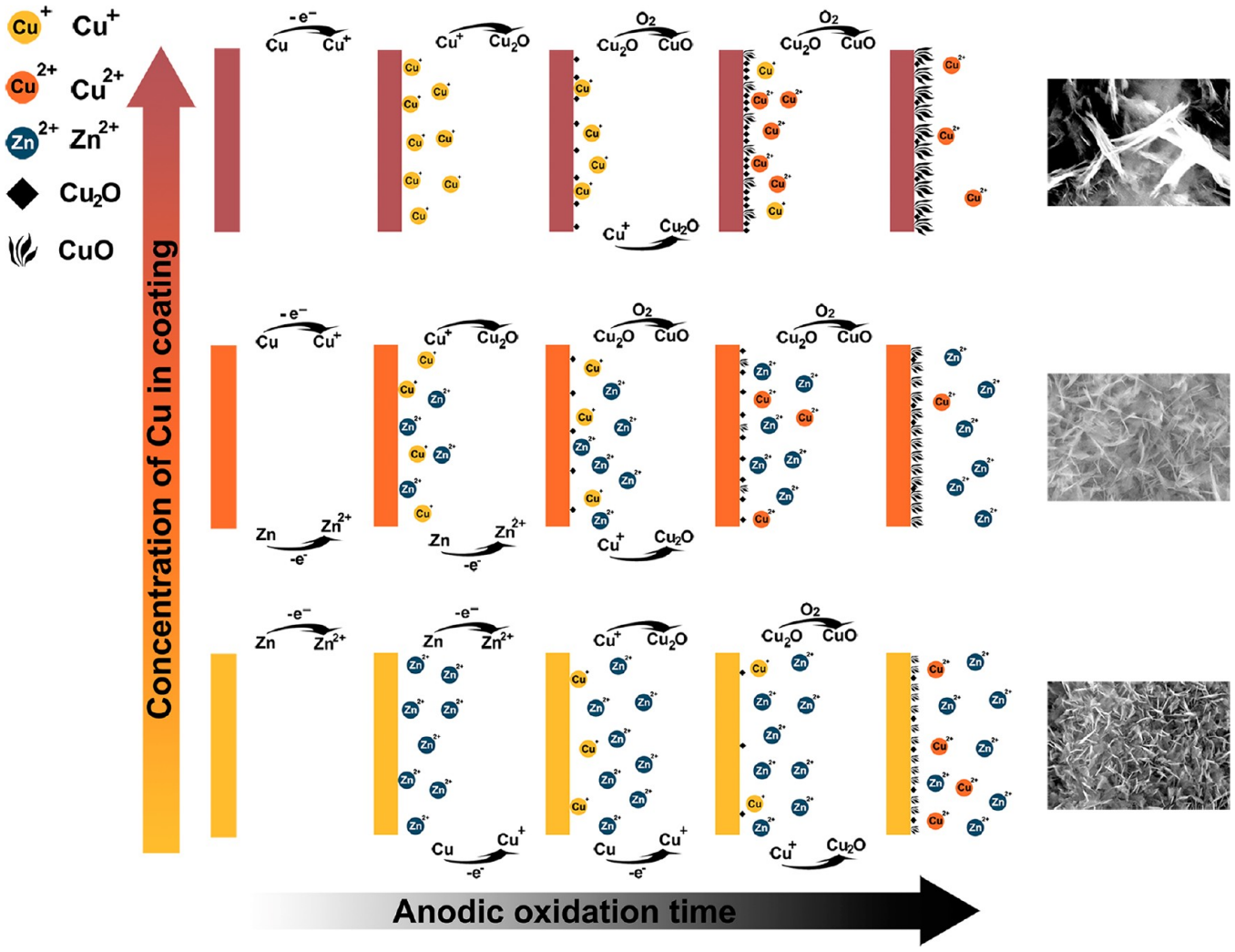

shown in Figure 6g was composed of the dense and uniform CuO which was evenly distributed on the surface. Careful inspection of the surface indicated that the surface contains a microstructure, nanostructure and hierarchical structure (Figure 6h). The numerous grooves in which the air can be trapped were found among the hierarchical CuO structures, which led to a high CA of 155.5 ± 1.3° and a low SA of 3° after modification with lauric acid. Furthermore, the CA change could be theoretically understood by the Cassie−Baxter equation[43]

$$\cos\theta = f_{sl}(1 + \cos\theta_0) - 1 \quad (1)$$

where θ and θ_0 represent the water CA on a rough surface and on a flat surface, respectively; f_{sl} is the fractional interfacial areas of solid/water on the surface, so $(1 - f_{sl})$ is the fractional areas of air/water. The value of θ_0 of smooth surface is almost changeless. Therefore, the larger or smaller surface roughness would increase f_{sl} and lead to the decrease in water CA (θ). But for the superhydrophobic surface, the trapped air can reduce the f_{sl} and produce large CA and small SA. Thus the water

dx.doi.org/10.1021/am3009949 | ACS Appl. Mater. Interfaces 2012, 4, 4348−4356

drops cannot penetrate into the grooves, but rather are suspended on the micro/nanostructured surface. The drops can hardly stick to the surface and will roll off quite easily from the surface with a slight inclination, even a slight vibration.

As depicted above, the Zn content in Cu−Zn coating was responsible for the achievement of superhydrophobicity. As the concentration of Zn^{2+} in bath increased, the Zn content in coating could increase and then affect the growth of featherlike CuO microstructures in electrochemical anodic treatment in NaOH. The optimal condition for fabricating superhydrophobic CuO surface is the molar ratio of Zn^{2+} to Cu^{2+} being 2.5:1 in bath.

3.3. Theoretical Growth Mechanism for CuO Architectures. On the basis of the above formation process of CuO film, the possible growth mechanism for featherlike CuO architectures was discussed. The mechanism illustration is depicted in Scheme 2. In our study, by using a relatively high concentration of NaOH and anodic potential, the pure Cu and Cu−Zn alloy coating (as anode) can be readily dissolved. The growth mechanism of featherlike CuO architectures is considered as consisting of the following steps: Step 1, dissolution of Cu (for pure Cu coating) and Zn (for Cu−Zn alloy coating) in the form of $Cu(OH)_2^-$ and $Zn(OH)_4^{2-}$, respectively; Step 2, generation and nucleation of Cu_2O; Step 3, dissolution of Cu in the form of $Cu(OH)_4^{2-}$; Step 4, generation and nucleation of CuO; Step 5, growth of CuO. These five steps might overlap temporally. Moreover, the five steps could be represented by the following reactions:[34,35,44−47]

$$Cu^+ + 2OH^- \rightarrow Cu(OH)_2^- \quad (2)$$

$$Zn + 4OH^- \rightarrow Zn(OH)_4^{2-} + 2e^- \quad (3)$$

$$2Cu(OH)_2^- \rightarrow Cu_2O + H_2O + 2OH^- \quad (4)$$

$$2Cu_2O + O_2 \rightarrow 4CuO \quad (5)$$

$$Cu^{2+} + 4OH^- \rightarrow Cu(OH)_4^{2-} \quad (6)$$

$$Cu(OH)_4^{2-} \rightarrow CuO + H_2O + 2OH^- \quad (7)$$

Reaction 2 first occurred on the pure Cu coating while reaction 3 first occurred on the Cu−Zn coating, so reaction 5 and 7 occurred on pure Cu coating earlier than that on Cu−Zn coating. This means that the growth time of CuO is much longer than that of Cu−Zn alloy coating. Obviously, the longer the growth time of CuO is, the larger the size of CuO is, resulting in the larger surface roughness. As shown in the SEM images inset in Scheme 2, the surface roughness decreased gradually with the prolonging of growth time of CuO. The surface exhibited the largest and the smallest roughness for pure Cu coating and Cu−Zn coating with high Zn content, respectively. In conclusion, the increase in Zn concentration in coating obstructed the progress of dissolving of Cu and the growth of CuO, resulting in the controllability of surface roughness.

3.4. Anticorrosion Effect. *Potentiodynamic Polarization.* Figure 7 shows the potentiodynamic polarization curves of bare magnesium alloy substrate, samples after electrodeposition, after electrochemical anodic treatment and the superhydrophobic surface in neutral 3.5 wt % NaCl solution. Different parameters such as corrosion potential (E_{corr}), corrosion current density (i_{corr}) and corrosion rate can be derived from Figure 7 using the Tafel extrapolation. It can be easily found

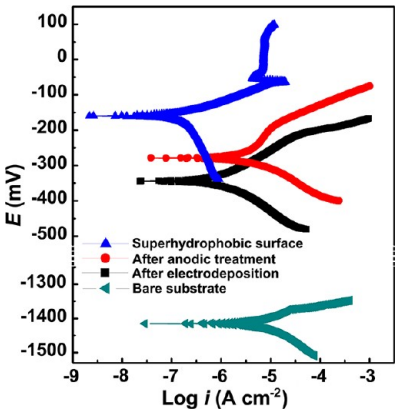

Figure 7. Potentiodynamic polarization curves of bare magnesium alloy substrate, samples after electrodeposition and after electrochemical anodic treatment and the superhydrophobic surface in neutral 3.5 wt % NaCl solution.

that the E_{corr} of the superhydrophobic surface is 1255 mV more positive than the bare substrate, 184 mV more positive than the sample after electrodeposition and 118 mV more positive than the sample after electrochemical anodic treatment and the i_{corr} of superhydrophobic surface (8.58×10^{-7} A cm^{-2}) decreased by more than 1 order of magnitude as compared to that of the bare substrate (6.73×10^{-6} A cm^{-2}), suggesting that the superhydrophobic surface has good corrosion resistance for magnesium alloy. Meanwhile, to express the difference of corrosion rate more clearly, the relative corrosion rate was used and the relative corrosion rates are depicted in Figure 8. The

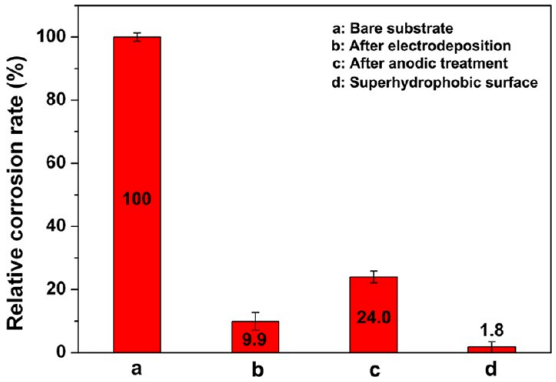

Figure 8. Relative corrosion rates of (a) bare magnesium alloy substrate, the samples after (b) electrodeposition and (c) anodic treatment, and (d) the superhydrophobic surface in neutral 3.5 wt % NaCl solution.

corrosion rate of bare magnesium alloy substrate was defined as 100%. It can be seen that the superhydrophobic surface presents the lowest corrosion rate, indicating that superhydrophobic CuO surface possessed a good anticorrosion property.

Interface Model and Anticorrosion Mechanism. As is well-known, water drops on a rough surface can have two states, Wenzel state[48] in which water drop will penetrate to the grooves of the rough surface, and Cassie-Baxter state[47] in which water drop is suspended on the surface. Generally, the superhydrophobic surface with a low sliding angle could be explained by the Cassie−Baxter state because the air trapped by micro/nanostructured surface can enhance the hydrophobic-

dx.doi.org/10.1021/am3009949 | ACS Appl. Mater. Interfaces 2012, 4, 4348−4356

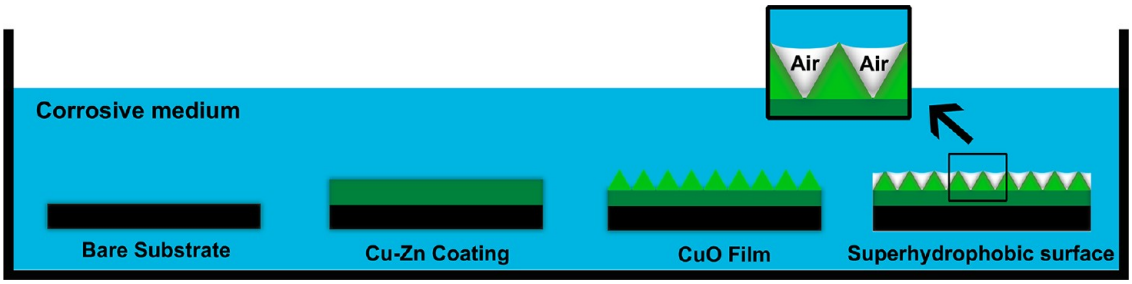

Figure 9. Interface model for anticorrosion mechanism of superhydrophobic surface in corrosive medium.

ity.[49,50] As depicted on above discussion, the water drop on the superhydrophobic CuO surface belonged to the Cassie−Baxter state.

In our potentiodynamic polarization tests, the interface showed a radically different condition that compared with other samples. We found that the superhydrophobic surface was immersed in NaCl solution; it was exceptionally bright when viewed from the side. But the bare substrate, Cu−Zn coating and CuO film were wetting. So we think the corrosion rate was affected not only by surface composition but also the interface condition. The interface conditions of different samples were presented in Figure 9. The bare substrate directly contacted with the medium and the corrosive ions, such as Cl^-, could easily penetrate to the magnesium alloy substrate and promote corrosive reactions arose, that leads to the highest corrosion rate. After electrodeposition process, the substrate was covered with Ni−P coating and Cu−Zn coating, which can block the penetration of ions and reduce the corrosive rate. For the CuO film, the corrosion rate increased compared with Cu−Zn coating because of the decrease in the film thickness and the formation of CuO "hills". The corrosive ions could penetrate to the substrate surface through the bottom of "valleys" more easily than the untreated Cu−Zn coating. Interestingly, after modification, the sample with superhydrophobic surface has the lowest corrosion rate. The superhydrophobic surface can easily trap air within the "valleys" between the "hills" in corrosive medium,[47] and the liquid forms a convex surface between the interface of the liquid and air for the capillary. Therefore, the ions can hardly reach the bare substrate surface for the obstructive effect of "air valleys" and generate the best corrosion inhibition ability.

Electrochemical Impedance Spectroscopy and Long-Term Stability. EIS is one of the most efficient and intensively used methods for investigation and prediction of corrosion protection.[51,52] EIS can be used to describe the impedance and the integrality of films. In this section, EIS was used to reveal the electrochemical corrosion behaviors and anticorrosion of the superhydrophobic surface by immersion tests. For a comparison, the anticorrosion properties of the films after electrodeposition and anodic treatment for bare substrate were presented. Figure 10 presents the Bode plots (impedance modulus |Z| as a function of frequency) with different immersion times in neutral 3.5 wt % NaCl solution. It can be easily found that the superhydrophobic surface possessed the highest impedance modulus |Z| at low frequency at 0 min, showing the best corrosion resistance for bare substrate compared with the films after electrodeposition and anodic treatment.

To investigate the stability of films over time in the corrosion solution, the superhydrophobic film and the films after electrodeposition and anodic treatment were immersed in the

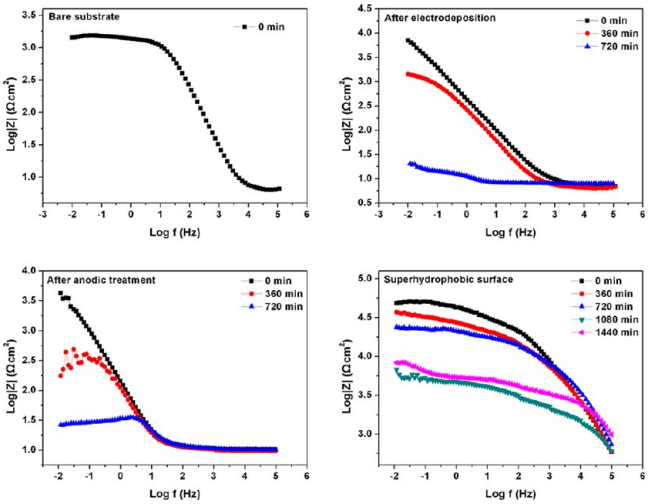

Figure 10. Bode plots of bare substrate, the sample after electrodeposition, after anodic treatment, and the superhydrophobic surface with different immersion times in neutral 3.5 wt % NaCl solution.

NaCl solutions from 0 to 1440 min. And the bare substrate was not immersed, because this could not give more information to gain the difference of the three films. With the prolonging of immersion time, the impedance modulus |Z| decreased for the film after electrodeposition and almost lost the corrosion protection at the immersion time of 720 min. For the film after anodic treatment, it lost the corrosion protection at the immersion time of 360 min. The decreasing impedance modulus |Z| indicated that the film was gradually broken with the prolonging of immersion time and the corrosion protection effect for substrate decreased. The corrosion protection of the sample after anodic treatment was much worse than that of the sample after electrodeposition, which could be due to the fact that the coating after anodic treatment became thinner and formed rough surface. For the superhydrophobic surface, the impedance modulus |Z| still remained a high value after immersion for 720 min and immersion for 1080 min, the impedance modulus |Z| continued to decline. When the immersion time was 1440 min, the impedance modulus |Z| decreased largely compared with that at 0 min, suggesting that the surface was broken. These results indicate that the superhydrophobic surface not only has good corrosion resistance for magnesium substrate but shows the best stability in corrosive medium compared with other two treatments.

3.5. Mechanical Stability. It is well-known that the mechanical stability is a highly important parameter for the practical application of materials. So the mechanical stability of superhydrophobic surfaces should be considered. In our study, the mechanical stability of the superhydrophobic surface was

dx.doi.org/10.1021/am3009949 | ACS Appl. Mater. Interfaces 2012, 4, 4348−4356

evaluated by using Scribe-Grid Test (ASTM D 3359-78) and microhardness test. Figure 11 shows the optical images of the

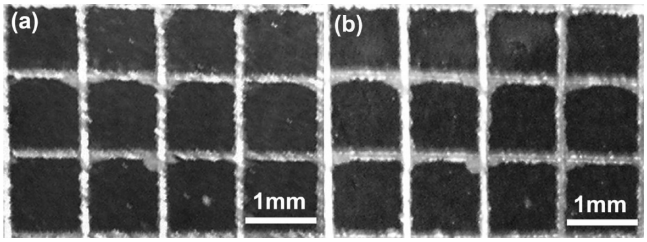

Figure 11. The optical images of the superhydrophobic CuO surface (a) before and (b) after the tape test.

superhydrophobic CuO surface before and after the tape test. The result shown in Figure 11b clearly indicated that the film had a good adhesion property. No delamination or detachment of the film at the edges and within the square lattice was observed. The adhesion of the resulting film to the substrate, measured according to ASTM D 3359-78 standard, corresponded to classification 4B. Besides, the microhardness of the resulting sample was measured using microhardness tester with a load of 1.9614 N and a dwell time of 30 s, showing that the resulting sample has a microhardness of 247 ± 19 HV. The results of mechanical stability clearly support that the as-prepared superhydrophobic CuO sample is stable enough to be possibly used in the environmental conditions.

4. CONCLUSIONS

In summary, a superhydrophobic CuO surface with special featherlike hierarchical structures was successfully fabricated on AZ91D magnesium alloy via a novel method in this study. The fabrication process was easily controllable by varying the coating composition. The results indicated that the optimal condition for fabricating superhydrophobic CuO surface was the molar ratio of Zn^{2+} to Cu^{2+} being 2.5:1 in bath. The superhydrophobic surface showed an excellent anticorrosion effect for magnesium alloy in neutral 3.5 wt % NaCl solution and good mechanical stability. Furthermore, the growth mechanism of featherlike CuO architectures and the interface model of anticorrosion mechanism were proposed in detail. It is believed that this facile, low-cost and large-area application method can offer an effective strategy and promising industrial applications for fabricating superhydrophobic surface on other metallic materials.

AUTHOR INFORMATION

Corresponding Author

*Tel: +86 023 68252360. Fax: +86 023 68254000. E-mail: liqingswu@163.com.

Notes

The authors declare no competing financial interest.

ACKNOWLEDGMENTS

This work was supported by the Fundamental Research Funds for the Central Universities (XDJK2012C011).

REFERENCES

(1) Wang, Z. W.; Li, Q.; She, Z. X.; Chen, F. N.; Li, L. Q. *J. Mater. Chem.* **2012**, *22*, 4097−4105.
(2) Nyström, D.; Lindqvist, J.; O'stmark, E.; Antoni, P.; Carlmark, A.; Hult, A.; Malmström, E. *ACS Appl. Mater. Interfaces* **2009**, *1*, 816−823.
(3) Jönsson-Niedziolka, M.; Lapierre, F.; Coffinier, Y.; Parry, S. J.; Zoueshtiagh, F.; Foat, T.; Yhomy, V.; Boukherroub, R. *Lab Chip* **2011**, *11*, 490−496.
(4) Zhou, Y. L.; Li, M.; Su, B.; Lu, Q. H. *J. Mater. Chem.* **2009**, *19*, 3301−3306.
(5) Jung, S.; Dorrestijn, M.; Raps, D.; Das, A.; Megaridis, C. M.; Poulikakos, D. *Langmuir* **2011**, *27*, 3059−3066.
(6) Xiao, J.; Chaudhuri, S. *Langmuir* **2012**, *28*, 4434−4446.
(7) Wang, P.; Zhang, D.; Qiu, R.; Hou, B. R. *Corros. Sci.* **2011**, *53*, 2080−2086.
(8) Liu, H. Q.; Szunerits, S.; Xu, W. G.; Boukherroub, R. *ACS Appl. Mater. Interfaces* **2009**, *1*, 1150−1153.
(9) Wang, L.; Guo, S. J.; Hu, X. G.; Dong, S. J. *Electrochem. Commun.* **2008**, *10*, 95−99.
(10) Ren, H. X.; Huang, X. J.; Yarimaga, O.; Choi, Y. K.; Gu, N. *J. Colloid Interface Sci.* **2009**, *334*, 103−107.
(11) Han, J. T.; Lee, D. H.; Ryu, C. Y.; Cho, K. *J. Am. Chem. Soc.* **2004**, *126*, 4796−4797.
(12) Huang, Z.; Zhu, Y.; Zhang, J.; Yin, G. *J. Phys. Chem. C* **2007**, *111*, 6821.
(13) Pan, Q. M.; Liu, J.; Zhu, Q. *ACS Appl. Mater. Interfaces* **2010**, *2*, 2026−2030.
(14) Chen, X. H.; Kong, L. H.; Dong, D.; Yang, G. B.; Yu, L. G.; Chen, J. M.; Zhang, P. Y. *J. Phys. Chem. C* **2009**, *113*, 5396−5401.
(15) Liu, H. Q.; Szanerits, S.; Pisarek, M.; Xu, W. G.; Boukherroub, R. *ACS Appl. Mater. Interfaces* **2009**, *9*, 2086−2091.
(16) Qian, B. T.; Shen, Z. Q. *Langmuir* **2005**, *21*, 9007−9009.
(17) Wang, Q.; Zhang, B. W.; Qu, M. N.; Zhang, J. Y.; He, D. Y. *Appl. Surf. Sci.* **2008**, *254*, 2009−2012.
(18) Kannarpady, G. K.; Khedir, K. R.; Ishihara, H.; Woo, J.; Oshin, O. D.; Trigwell, S.; Ryerson, C.; Biris, A. S. *ACS Appl. Mater. Interfaces* **2011**, *3*, 2332−2340.
(19) Han, J. T.; Kim, S. C.; Karim, A. *Langmuir* **2007**, *23*, 2608−2614.
(20) Tiwari, M. K.; Bayer, I. S.; Jursich, G. M.; Schutzius, T. M.; Megaridis, C. M. *ACS Appl. Mater. Interfaces* **2010**, *2*, 1114−1119.
(21) Fan, G. L.; Li, F. *Chem. Eng. J* **2011**, *167*, 388−396.
(22) Pei, M. D.; Wang, B.; Li, E.; Zhang, X. H.; Song, X. M.; Yan, H. *Appl. Surf. Sci.* **2010**, *256*, 5824−5827.
(23) Liu, J. P.; Huang, X. T.; Li, Y. Y.; Li, Z. K.; Chi, Q. B.; Li, G. Y. *Solid State Sci.* **2008**, *10*, 1568−1576.
(24) Zhang, X.; Guo, Y. G.; Zhang, P. Y.; Wu, Z. S.; Zhang, Z. J. *Mater. Lett.* **2010**, *64*, 1200−1203.
(25) Wang, G. Y.; Zhang, T. *J. Colloid Interf. Sci.* **2012**, *377*, 438−441.
(26) Zheng, M. Y.; Wu, K.; Liang, M.; Kamado, S.; Kojima, Y. *Mater. Sci. Eng., A* **2004**, *372*, 66−74.
(27) Huo, H. W.; Li, Y.; Wang, F. H. *Corros. Sci.* **2004**, *46*, 1467−1477.
(28) Gray, J. E; Luan, B. *J. Alloys Compd.* **2002**, *336*, 88−113.
(29) Shih, T. S.; Liu, J. B.; Wei, P. S. *Mater. Chem. Phys.* **2007**, *104*, 497−504.
(30) Gao, L. C.; McCarthy, T. J. *Langmuir* **2007**, *23*, 3762−3765.
(31) Zhao, Y.; Tang, Y. W.; Wang, X. G.; Lin, T. *Appl. Surf. Sci.* **2010**, *256*, 6736−6742.
(32) Pithawalla, Y. B.; El-Shall, M. S.; Deevi, S. *Scripta Mater.* **2003**, *48*, 671−676.
(33) Mukhopadhyay, N. K.; Mukherjee, D.; Bera, S.; Manna, I.; Manna, R. *Mater. Sci. Eng. A* **2008**, *485*, 673−680.
(34) Zhao, W. Y.; Lu, W. Y.; Yang, H. B.; Tian, C. J.; Ge, R. X.; Wang, C. J.; Liu, Z. L.; Zhang, Y. Y.; Li, M. H.; Li, Y. X. *Appl. Surf. Sci.* **2010**, *256*, 2269−2275.
(35) Qiu, H. J.; Lu, L.; Huang, X. R.; Qu, Y. B. *Electrochim. Acta* **2010**, *56*, 291−296.
(36) Liu, X. W.; Geng, B. Y.; Du, Q. B.; Ma, J. Z.; Liu, X. M. *Mater. Sci. Eng. A* **2007**, *448*, 7−14.
(37) Lee, S. M.; Kim, K. S.; Pippel, E.; Kim, S.; Kim, J. H.; Lee, H. J. *J. Phys. Chem. C* **2012**, *116*, 2781−2790.
(38) Yin, M.; Wu, C. K.; Lou, Y. B.; Burda, C.; Koberstein, J. T.; Zhu, Y. M.; O'Brien, S. *J. Am. Chem. Soc.* **2005**, *127*, 9506−9511.

(39) Yao, W. T.; Yu, S. H.; Zhou, Y.; Jiang, J.; Wu, Q. S.; Zhang, L.; Jiang, J. *J. Phys. Chem. B* **2005**, *109*, 14011−1406.
(40) Basu, M.; Sinha, A. K.; Pradhan, M.; Sarkar, S.; Negishi, Y.; Pal, T. *J. Phys. Chem. C* **2011**, *115*, 20953−20963.
(41) Wang, S.; Feng, L.; Jiang, L. *Adv. Mater.* **2006**, *18*, 767−770.
(42) Verplanck, N.; Coffinier, Y.; Thomy, V.; Boukherroub, R. *Nanoscale Res. Lett.* **2007**, *2*, 577−596.
(43) Cassie, A. B. D.; Baxter, S. *Trans. Faraday Soc.* **1944**, *40*, 546−550.
(44) Yu, L. G.; Zhang, G. M.; Li., S. Q.; Xi, Z. H.; Guo, D. Z. *J. Crystal Growth* **2007**, *299*, 184−188.
(45) Zhang, Y. F.; Yu, X. Q.; Zhou, Q. H.; Chen, F.; Li, K. N. *Appl. Surf. Sci.* **2010**, *256*, 1883−1887.
(46) Fan, G. L.; Li., F. *Chem. Eng. J.* **2011**, *167*, 388−396.
(47) Liu, Y.; Chu, Y.; Li, M. Y.; Li, L. L.; Dong, L. H. *J. Mater. Chem.* **2006**, *16*, 192−198.
(48) Wenzel, R. N. *J. Ind. Eng. Chem.* **1936**, *28*, 988−994.
(49) Liu, L. J.; Zhao, J. S.; Zhang, Y.; Zhao, F.; Zhang, Y. B. *J. Colloid Interf. Sci.* **2011**, *358*, 277−283.
(50) Hong, Y. C.; Cho, S. C.; Shin, D. H.; Lee, S. H.; Uhm, H. S. *Scr. Mater.* **2008**, *59*, 776−779.
(51) Zhang, S. Y.; Li, Q.; Chen, B.; Yang, X. K. *Electrochim. Acta* **2010**, *55*, 870−877.
(52) Liu, T.; Yin, Y. S.; Chen, S. G.; Chang, X. T.; Cheng, S. *Electrochim. Acta* **2007**, *52*, 3709−3713.